Catalysis Today 175 (2011) 245–255

Contents lists available at ScienceDirect

Catalysis Today

journal homepage: www.elsevier.com/locate/cattod

Study on the direct decomposition of nitrous oxide over Fe-beta zeolites: From experiment to theory

Biaohua Chen, Ning Liu, Xingyong Liu, Runduo Zhang*, Yaping Li, Yingxia Li, Xiuliang Sun

State Key Laboratory of Chemical Resource Engineering, Beijing University of Chemical Technology, Beijing 100029, China

ARTICLE INFO

Article history:
Received 23 September 2010
Received in revised form 17 February 2011
Accepted 6 April 2011
Available online 14 May 2011

Keywords:
Nitrous oxide
BEA zeolite
DFT
Catalytic decomposition
Mechanism

ABSTRACT

N_2O direct decomposition over Fe-beta zeolite prepared by wet ion-exchange (WIE) was systematically investigated based on the experimental and theoretical studies in this paper. Both isolated iron ions in the charge compensation positions and highly dispersed FeO_x-like crystallite were verified by means of H_2-TPR. Catalytic performances of various Fe-BEA zeolites with diverse iron contents were thereafter studied. The results showed that: (1) the catalytic activity of bare beta zeolite was significantly promoted via ion-exchange; (2) no obvious further increase in *de*N_2O activity was observed for Fe-beta samples with iron contents higher than 1%. Two kinds of reaction mechanism, with respective formation of oxygen (O_2) or nitrogen oxide (NO_x) intermediate, for the direct decomposition of N_2O over Fe-beta zeolite (noted as Fe-Z) were proposed according to the N_2O-TPD, NO_2-TPD, N_2-TPD, N_2O-TPSR, and in situ DRIFTS investigation and density functional theory (DFT) study. The corresponding energy calculations for O_2-formation mechanism revealed that O_2 desorption was the rate determining step with an energy barrier of 63.20 kcal/mol. Another mechanism with NO formation was also simulated by DFT calculations, whose energy calculations indicated that the formation of Fe-Z-$(NO)_2$ was the main pathway for NO generation with an energy barrier of 26.92 kcal/mol.

1. Introduction

Nitrous oxide is classified as one kind of greenhouse gases with global warming potential (GWP) as much as 310 [1], making a major contribution (about 6%) to global climate change [2]. A large and increasing amount of N_2O is generated from the chemical industries for the production of adipic acid and nitric acid. N_2O emission control has therefore become one of the great challenges for environmental protection. Some methods including thermal decomposition (TD) [3], directly catalytic decomposition (DCD) [4–12] and selectively catalytic reduction (SCR) [13–16] have been tried to eliminate the harmful N_2O. Among them, the directly catalytic decomposition is regarded as the simplest and most effective way for N_2O abatement with noble metals as the common catalysts due to their high intrinsic activities for N_2O decomposition [17]. However, precious metal catalysts were readily deactivated by unfavorable molecules (e.g. H_2O, NO) present in the tail gases of adipic acid and nitric acid plants [18,19].

Recently Fe-zeolites have attracted great attention because of their excellent catalytic performances for N_2O decomposition [5–16] even in the presence of steam [12]. For Fe-zeolites it is generally accepted that surface iron species form the core of catalytic sites for N_2O decomposition and different preparation methods will lead to diverse types of iron species. Actually, the exact nature of the active Fe sites remains a matter of debate, and a wide variety of Fe species has been identified in Fe-zeolites, such as isolated Fe^{3+} and FeO^+ cations, di-iron oxo-cations with possible μ-hydroxo or de-η-hydroxo groups and peroxide bridges $(FeO_x)_n$ nanoclusters and small Fe_2O_3 aggregates [14,20,21].

Pirngruber et al. [22] studied N_2O direct decomposition over Fe-ZSM-5 zeolites modified by different methods including wet ion-exchange (WIE), chemical vapor deposition (CVD) and hydrothermal synthesis (HT), and found that the dominating iron species in the above three kinds of Fe-ZSM-5 zeolites were isolated iron centers (WIE), iron oxide clusters of 2–4 iron atoms (CVD) and larger iron oxide clusters (HT). Rivallan et al. [23] investigated N_2O decomposition over Fe-ZSM-5 prepared by WIE and demonstrated that low coordinated and isolated Fe^{2+} sites were the most active sites for N_2O decomposition. It was also reported that these Fe^{2+} active sites could be formed during the activation under an inert atmosphere or in vacuum [24,25]. Moreover, Pirngruber et al. [5] pointed out that N_2O decomposition activity depended strongly on the extent of autoreduction of the catalysts during their pretreatments by a He stream at high temperature and that ion-exchanged catalysts usually displayed a relatively high turnover frequency. Li and co-workers [26] proposed that ferrous

* Corresponding author at: State Key Laboratory of Chemical Resource Engineering, Beijing University of Chemical Technology, Box 266, Beijing 100029, China. Tel.: +86 10 64412054; fax: +86 10 64419619.
E-mail address: zhangrd@mail.buct.edu.cn (R. Zhang).

0920-5861/$ – see front matter © 2011 Elsevier B.V. All rights reserved.
doi:10.1016/j.cattod.2011.04.010

ions in the high-temperature-treated Fe-ZSM-5 catalyst showed a much higher reactivity in nitrous oxide decomposition as compared to Fe^{3+} sites. Furthermore, Fe^{2+} species were most likely associated with the iron–aluminium species formed upon the high-temperature treatment.

The mechanism of N_2O decomposition likely involves an adsorbed oxygen intermediate called "α-oxygen" [27]. Additionally, the desorption of O_2 is considered as the rate-determining step [26]. Although all types of iron species contribute to O_2 desorption, a fast pathway of O_2 desorption was dominated upon isolated iron sites, whereas a slow pathway of O_2 desorption was accordingly associated with the high iron loadings [22]. Two points for N_2O direct decomposition based on Fe-ZSM-5 zeolite were commonly accepted: (1) oxygen formation was through the migration of α-O from two active sties [24]; (2) N_2O decomposition and oxygen evolution occurred at the same active site [25].

Pérez-Ramírez et al. [28] studied the effect of NO on N_2O decomposition over Fe-based zoelites, showing that NO had an obviously positive effect on the decomposition of N_2O and no inhibition was found as the NO/N_2O feed ratio was increased to as high as 10. Then, a model was proposed to explain the NO-assisted N_2O decomposition. The site for NO adsorption was different from that for N_2O deposition. Adsorbed NO could readily capture the oxygen atom from the N_2O molecule to form the adsorbed NO_2. As a result, the N_2O decomposition process was accelerated.

Fe-beta zeolite acted as another kind of efficient catalyst for the direct decomposition of N_2O [6] and for the SCR of N_2O by NH_3 [15] and CH_4 [16] exhibiting superior activity in comparison with Fe-ZSM-5 zeolite due to its special topology of a widely open three-dimensional channel structure and 12-membered ring aperture. Øygarden and Pérez-Ramírez [29] compared activities of various commercial zeolites (MFI, FER, BEA, MOR, FAU) with similar Si/Al ratios for N_2O direct decomposition. It was found that Fe-BEA was the most effective material for this reaction. Pieterse et al. [30] studied the hydrothermal stability of Fe-ZSM-5 and Fe-BEA prepared by WIE for N_2O decomposition and announced that Fe-BEA zeolite had a better hydrothermal stability. Although some work for N_2O direct decomposition by using beta-type zeolites has been done as previously reported [29,30], more detailed investigations are still necessary because the related studies (especially for mechanism assumption) are so far not well established.

Computational chemistry based on density functional theory (DFT) is widely used for mechanism study because of its accurate simulation of chemical reaction processes. By means of DFT calculation, Lund [31] compared two kinds of Fe-ZSM-5 models, 5T and two full 10-membered zeolite rings, with $[FeO]^+$ as the active center for N_2O decomposition, and declared that the longer-range interactions with the zeolite channel walls did not significantly affect the energies of the mechanistic steps studied. Fellah and Onal [32] calculated the mechanism of N_2O decomposition over Fe-, Co-ZSM-5 using a relaxed model $[(SiH_3)_4AlO_4M]$ (M = Fe, Co) with $[M]^+$ as the active center, proving that O_2 desorption was the rate-limiting step for both clusters. Yakovlev [33] studied the direct decomposition catalyzed by 5-coordinated transition metal ions (Fe, Co, and Rh) modeled as $M(OH_3)(H_2O)_2$ using the DFT method, and the calculation results were in accordance with the experimental data. In light of the DFT calculation, Heyden comparatively studied the mechanism of N_2O decomposition on hydrated and dehydrated mononuclear iron sites in Fe-ZSM-5 with a 5T model of $[(SiH_3)_4AlO_4(FeO)]$ and $[FeO]^+$ as the active centers [34,35]. Nevertheless, DFT studies on N_2O decomposition over Fe-BEA zeolites are scarce in the literature.

In the present paper, N_2O decomposition behaviors over Fe-BEA prepared by WIE were investigated. The corresponding decomposition mechanisms were studied by not only experimental methods such as N_2O-temperature programmed desorption (TPD), NO_2-TPD, N_2-TPD, N_2O-temperature programmed surface reaction (TPSR), diffuse reflectance infrared Fourier transform spectra (DRIFTS), and activity test, but also by theoretical study via computational chemistry based on a density functional theory (DFT) in which energies for adsorption/desorption, activation energy barrier and reaction enthalpy were calculated and the energy profiles were depicted.

2. Experimental and computational methods

2.1. Experimental method

2.1.1. Catalyst preparation

The parent beta zeolite with a Si/Al ratio of 30 was presently prepared by dynamic hydrothermal synthesis using tetraethyl ammonium hydroxide (TEAOH) as a template. The solution for zeolite synthesis was prepared by mixing silica powder, sodium aluminate (45 wt% Al_2O_3), sodium hydroxide (AR), tetraethyl ammonium hydroxide (20 wt% in water) and deionized water with molar ratios of Si/Al = 30, H_2O/Si = 10, Na^+/Si = 0.15, TEAOH/Si = 0.1. This mixture was stirred at 200 r/min for 1 h in the autoclave, then aged at 393 K for 24 h, and finally crystallized at 423 K for 48 h. After being ion-exchanged with ammonium nitrate solution (0.1 M) for three times at 353 K and subsequently calcined at 823 K for 4 h in air, the as-synthesized sample converted into the H-form one.

Fe-beta zeolites modified by ferric nitrate with different iron loadings (0.25%, 0.5%, 1%, 1.5%, 2%, and 3%) were prepared by WIE. The parent H-beta zeolites were firstly mixed with iron salt solution and continuously stirred at 373 K for 3 h. After being filtrated and washed by deionized water, the samples were dried at 373 K for 12 h. Finally, the Fe-beta zeolites were obtained after a further calcination at 823 K for 4 h.

2.1.2. Characterization for physicochemical properties

The chemical composition of catalysts was determined by atomic absorption spectroscopy (AAS) via a Hitachi Z-8000 spectrometer. The samples were dissolved into HCl (98%) solution mixing with drops of HF.

The X-ray diffraction (XRD) patterns have been recorded in the 2θ ranges from 5 to 45° using X-ray diffractometer (Rigaku, D/max2500VB2) with a radiation of Cu Kα (λ = 1.5406 Å). The crystal phases were confirmed according to JCPDS reference while the crystallite sizes were calculated on the basis of Scherrer equation.

The specific surface area (S_{BET}) of the solids was measured via a Sorptomatic 1990 instrument (Thermo Electron) through nitrogen adsorption/desorption at 77 K and was calculated by the Brunauer–Emmett–Teller (BET) method. Micropore volume (V_{micro}) was obtained by using *t*-plot method as well as the pore size distribution of the solids was determined according to Horvath–Kavazoe equation.

H_2-temperature programmed reduction (TPR) was performed using Thermo Electron TPD/R/O 1100 Series instrument equipped with a thermal conductivity detector (TCD). Before study, samples were in turn pretreated by the following procedures: (1) heated at 773 K for 1 h in a He (>99.999%) stream; (2) oxidized by O_2 (9.98% in He) for 30 min; (3) cooled down to 348 K under above atmosphere (9.98% O_2/He) (4) purged by He (>99.999%) for 30 min at 348 K. H_2-TPR started with a ramp of 10 K/min from 348 to 1273 K. The flow rate of reducing gas (5.06% H_2 balanced by N_2) was 20 ml/min.

2.1.3. Characterization for mechanism study

Diffuse reflectance infrared Fourier transform spectra (DRIFTS) were obtained using a Bruker TENSOR 27 system equipped with a MCT detector. The catalyst (~1 mg) diluted by KBr and ground in an agate mortar was placed into the diffuse reflectance cell (Harrick)

fitted with KBr windows and a heating cartridge that allowed samples to be heated up to the desired temperature. The investigated samples were in situ activated by helium for 1 h at 773 K before DRIFTS measurements. All spectra were collected with a resolution of 4 cm^{-1} and an accumulation of 100 scans.

N_2O-, NO_2-, and N_2-temperature programmed desorption (TPD) over Fe-beta-1% zeolite has been performed through a fix-bed reactor system equipped with a quadrupole mass spectrometer (MS) (OmniStar MS 200). Before each run the catalyst was activated in the helium stream (>99.999%, 20 ml/min) at 773 K for 2 h, and then cooled down to 573 K. Subsequently, the catalyst was exposed to 20 ml/min of N_2O (4 vol% in He) or NO_2 (2 vol% in He) or N_2 (1 vol% in He) for 1 h before further cooling down to ambient temperature under the same atmosphere. After the catalyst was purged by He (>99.999%, 20 ml/min) for 60 min at room temperature in order to remove any physisorbed molecules, TPD was performed with a ramp rate of 5 K/min. The following signals, indicating mass numbers, were simultaneously detected by MS through multiple ion detection (MID): 14 (N_2), 28 (N_2), 30 (NO), 32 (O_2), 44 (N_2O), and 46 (NO_2).

N_2O-temperature programmed surface reaction (TPSR) has also been conducted by a similar system as above described. After the helium activation of 25 mg catalyst, TPSR was performed with a ramp of 5 K/min. The feed gases of N_2O and He were mixed by using mass flow controller with a molar ratio of N_2O/He = 35/65 and a GHSV of 4000 h^{-1}. The outlet gases were simultaneously recorded by both MS and a five-way infrared gas analyzer (SIEMENS VS5067-5D).

2.1.4. Activity measurements

Catalytic tests for N_2O decomposition were performed through a fixed-bed reactor (Φ7 mm × 1 mm × L300 mm) with the reaction temperature ranging from 573 to 773 K. 250 mg of pelletized catalyst with particle sizes of 250–425 μm was placed in the constant temperature zone of a vertical tubular reactor. The catalyst was in situ pretreated by a helium stream (>99.999%) at 773 K for 3 h for activation. Afterwards a gas mixture consisting of 35 vol% N_2O balanced by 65 vol% He was made according to the components of tail gas from the related industrial plants as previously described [36] and fed into the reactor under atmospheric pressure. A total flow rate of 60 ml/min was employed for the activity test, corresponding to a GHSV of 4000 h^{-1}. The gaseous products were discontinuously analyzed by gas chromatograph (GC-4000A) equipped with a TCD and a TDX-01 column for the separation of N_2O, N_2 and O_2. A five-way gas analyzer (SIEMENS VS5067-5D) was also used to monitor the NO concentration in the effluent. This analyzer has infrared optical sensor and is able to detect NO, CO, CO_2, O_2 and HCs. Steady-state tests were conducted isothermally every 10 K along with the reaction temperature ascending from 573 K to the temperature at which 100% N_2O conversion was achieved. The N_2O conversion is designed as follows:

$$\text{conversion of } N_2O \ (\%) = \frac{[N_2]}{[N_2O] + [N_2]} \times 100\% \quad (2.1)$$

where $[N_2O]$ and $[N_2]$ are the concentration of N_2O and N_2, respectively, as measured by the chromatograph.

2.2. Zeolite structure model and computational method

Quantum calculation of density functional theory (DFT) [37] was used to investigate the mechanism of N_2O decomposition over Fe-beta zeolite that was simulated by a 5T model [$(SiH_3)_4AlO_4Fe$] during DFT calculations. The framework structure of the 5T model was derived from the beta zeolite structure (which was contained in the database of MS Modeling 4.0 package of Accelrys Inc. as an all silica model) with one Al atom replacing one Si atom and leaving four Si atoms in BEA crystal model. According to the preparation method of Fe-beta zeolite in this study, the activity center was simulated as mononuclear iron cations compensating AlO_4^- via ion-exchanging with the H proton of Brönsted acid. In our previous paper [38], the energy associated with placing an aluminium atom in the tetrahedral site of BEA was theoretically studied. It was found that the T5 site was the most favorable site for Al substitution. Brönsted acidity of the T5 site was also investigated by Ref. [38], knowing that the Al5(T5)-O-Si(T9) site had the highest acidity. Consequently, a model of the 5T-Fe-beta zeolite was accordingly established with atomic Al situated at the T5 site and active center Fe compensating AlO_4^- at the Al5(T5)–O–Si(T9) site.

Pirngruber et al. [5] studied the mechanism of N_2O direct decomposition over Fe-ZSM-5 zeolite and further compared with the mechanism proposed by Heyden et al. [34]. It was reported that the initial activity center of Fe-ZSM-5 prepared by WIE should be the iron species in a reduced status because the catalyst could be activated by He treatment at high temperature before starting the reaction. Therefore, the active center of the 5T-Fe-beta model in the present paper was simulated as $[Fe]^+$. The dangling bonds of the 5T-Fe-beta model were terminated by H atoms located 1.49 Å from each terminal Si atom in the direction towards the substituted O atom in the zeolite matrix.

Computations in this work were performed by using the Gaussian 03 software package [39]. The algorithm of DFT was combined with the Becke three-parameter hybrid method, by using the LYP correlation function (B3LYP) [40,41]. The core electrons of the Fe atom were represented by the LANL2DZ effective core potential (ECP), and its valence electrons were described by the LANL2DZ basis set. For atoms of Si, Al, O, N and H, the common basis set 6-31G(d) was used during the calculations of geometry optimization (GO), transition state (TS) and intrinsic reaction coordinate (IRC), while the high level basis set 6-311++G(d,p) was used for energy calculation.

Before geometry optimization the single point energy (SPE) was calculated to decide the proper spin multiplicity (SM), and the SM with the lowest SPE was used in this work. Charges of all the clusters were taken as neutral during the quantum calculations. Atoms of H and Si were all kept frozen during GO and TS calculations in order to maintain the configuration of BEA, while other cluster atoms were kept relaxed.

Energy calculation was based on the optimized cluster and corrected by zero point energy (ZPE) through frequency calculation in which the basis set was the same as that used in GO calculation. Adsorption and desorption energy calculations were additionally corrected by basis set superposition error (BSSE). Reaction enthalpy was calculated at 298.15 K and 1.0 atm.

For the first N_2O molecule decomposition over Fe-beta zeolite (Fe-Z), the only adsorption mode studied in this paper was that of N_2O adsorption via O onto the active center Fe of Fe-Z, as opposed to via N. Translate state clusters in the present paper were testified by both frequency calculations, having only one imaginary frequency, and IRC calculations.

3. Results and discussion

3.1. Characterization of Fe species loaded on the Fe-beta zeolites

The Fe content, BET surface area, crystallite size, and pore volume & average diameter of the prepared samples were listed in Table 1. Fe contents of the prepared samples established by AAS were close to the nominal values. A typical structure of beta-typed zeolite for all samples prepared by WIE was confirmed by XRD patterns (not shown). This crystal structure was well maintained even after Fe ion-exchange. Furthermore, no characteristic peak belong-

Table 1
Chemical composition, BET surface areas, pore volume, pore average diameter, and crystallize size of the investigated samples.

Sample	Fe(wt%)[a]	BET surface area (m^2/g)	V_{micro} (cm^3/g)	Pore average diameter (nm)	Crystallite size (nm)[b]
H-beta	0	406	0.2997	1.437	7.587
Fe-beta-0.25%	0.23	419	0.3032	1.258	8.488
Fe-beta-0.5%	0.42	436	0.3494	1.344	9.129
Fe-beta-1%	0.92	438	0.3182	1.274	9.493
Fe-beta-1.5%	1.35	440	0.3428	1.642	8.279
Fe-beta-2%	1.82	463	0.3694	1.258	8.349
Fe-beta-3%	2.75	501	0.4026	1.292	8.932

[a] Measured by AAS.
[b] Calculate by Scherrer equation.

ing to iron oxides was observed in all the diffraction patterns with the Fe loading varying from 0.25% to 3%, indicating that the Fe component was well dispersed over the molecular sieve. However, the existence of tiny FeO_x species which are XRD invisible or iron content below the detection limit cannot be totally excluded.

H_2-TPR experiments were conducted over both H-beta and Fe-beta zeolites with Fe contents of 0.25%, 0.5%, 1%, 1.5%, 2%, and 3%, as depicted in Fig. 1. The absence of TPR peak in the case of H-beta sample suggested good stability of the zeolite framework under a reducing atmosphere at temperatures as high as 1273 K. TPR spectra for the Fe-containing zeolites (apart from Fe-beta-2% sample) show similar profiles representing two superimposed H_2 reducing peaks between 423 and 773 K. These two peaks were likely corresponding to the reduction of Fe^{3+} to Fe^{2+} in ion-exchange positions of zeolites according to the literature [7,8]. The additional peaks between 773 and 1073 K were probably due to the reduction of iron-oxides clusters [9,10,20]. As reported by Munteanu et al. [42], the peaks between 773 and 900 K in the TPR curves of Fe-beta-2% and Fe-beta-3% samples were assigned to the reduction of Fe_3O_4 to FeO and the peak at 940 K in the curve of Fe-beta-3% sample was assigned to the further reduction of FeO to Fe^0.

H_2-TPR revealed that two kinds of Fe species existed on the zeolite: isolated Fe^{3+} ions, formed via ion-exchange with proton hydrogen of Brönsted acid by valence bond compensation through the WIE, and fine FeO_x species (e.g. Fe_3O_4, oxygen-bridged binuclear Fe species or mononuclear Fe species). As the Fe content was low, it mainly existed in the form of Fe^{3+} ions on the zeolite as shown in the TPR plot of Fe-beta-0.25% (the peaks at 533 and 673 K) and Fe-beta-0.5% (the peak at 683 K) in Fig. 1. Further increasing the Fe loading, the reducing peak of $FeO_x \rightarrow FeO$ became significant as discerned from the TPR curves of Fe-beta-2% (the peak at 800 K) and Fe-beta-3% (the peak at 840 K). In the spectrum of Fe-beta-3% a special peak with a maximum at 940 K is probably due to a further reduction of FeO to metallic Fe on the catalyst surface. Isolated Fe^{3+} coordinated with the zeolite framework is thought to be the active center for the direct decomposition of nitrous oxide, while rather poor activity of iron oxide outside the zeolite lattice is assumed for this reaction as reported by Pérez-Ramírez et al. [11].

3.2. Catalytic activity evaluation

The conversion of N_2O as a function of temperature for H-beta and Fe-beta zeolites was shown in Fig. 2. It was found that the catalytic activity of beta-type zeolites could be significantly promoted by means of Fe loading showing an obvious enhancement in N_2O conversion with the full-conversion temperature of Fe-beta-1% zeolite being 130 K lower than that of H-beta zeolite. In addition, further increase in *de*N_2O activity upon the increasing loading was marginal for Fe-beta samples with iron contents higher than 1%. Accordingly, we correlated the catalytic behaviors with the status of Fe species. Fe species might be well dispersed as an ionic form at its content below 1%, as verified by H_2-TPR, leading to a monotonous increase of N_2O conversion along with more Fe loading. The increase of loading more than 1% could lead to the appearance of FeO_x phase (see Fig. 1), which was believed to be less active for N_2O decomposition, as the amount of iron exceed that needed for a monolayer coverage. The further increase in activity associated with the Fe loadings above 1% was hardly observed although the amount of isolated Fe^{3+} ions could be successively improved via more Fe loading, based on a quantitative analysis of

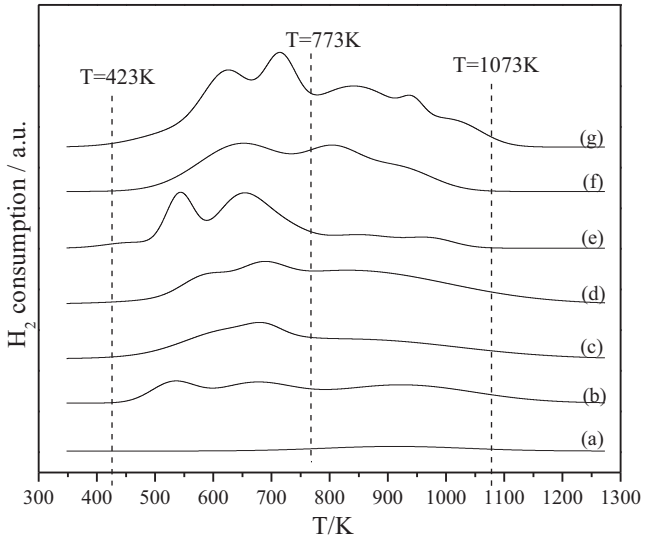

Fig. 1. H_2-TPR profiles for (a) H-beta and Fe-beta zeolites with the iron content of (b) 0.25%, (c) 0.5%, (d) 1%, (e) 1.5%, (f) 2%, (g) 3%.

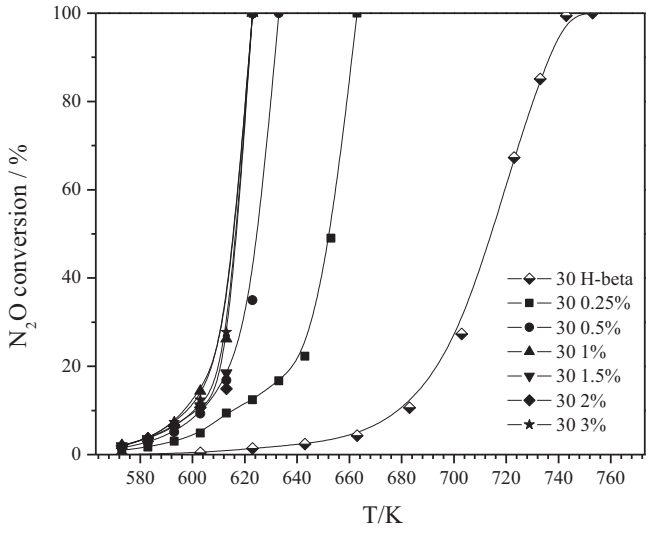

Fig. 2. N_2O conversion as a function of temperature over a series of Fe-beta zeolites, conditions: 35 vol% N_2O/He, GHSV = 4000 h^{-1}.

the corresponding TPR peaks in Fig. 1. It was thus believed that the reaction was mainly controlled by internal mass transfer (as Fe loading above 1%) instead of kinetic (as Fe loading below 1%).

3.3. Mechanism study

3.3.1. In situ diffuse reflectance infrared Fourier transform spectra (DRIFTS)

The DRIFTS of N_2O (4vol% in He) adsorbed on the Fe-beta-1% zeolite at 573 K as a function of exposure time were plotted in Fig. 3A. Once, Berlier et al. [43], respectively, assigned the bands at 2218 and 2235 cm^{-1} (with a shoulder at 2000 cm^{-1}) to the physisorbed N_2O and the chemisorbed N_2O on the Fe^{2+} centers. In the literature, the bands at 2208 and 2238 cm^{-1} were ascribed to the ν(N–N) stretching modes [44] and the band at 1300 cm^{-1} was associated with ν(N–O) stretching modes [45]. It was clearly seen from Fig. 3A that the intensities of bands at 2208–2218 and 2235 cm^{-1} were increased as the exposure time was prolonged, implying some chemisorbed species were formed and further accumulated over the zeolite, although some reports suggested that these bands might correspond to the infrared vibrations of the N_2O molecule in the gas phase [46]. Accordingly, the bands at 2208–2218 and 2235 cm^{-1} appearing in Fig. 3A were attributed to the weakly chemisorbed (possibly overlapping with some physisorbed) N_2O. The slight bands at 1275 and 1300 cm^{-1} were likely due to a contribution of ν(N–O) stretching modes from either adsorbed N_2O or some newly generated NO species after N_2O chemisorption.

The DRIFTS for Fe-beta-1% zeolite with an exposure to 4 vol% N_2O/He at different temperatures were plotted in Fig. 3B. Subsequently, the area of IR bands at 2208–2218 and 2235 cm^{-1} as a function of temperature was also shown as an inserted figure. The intensities of infrared bands of N_2O (2208–2218, 2235 cm^{-1}) diminished gradually with the temperature rising from 323 to 673 K (especially at <473 K) and these bands almost vanished at 673 K. This suggests that the physisorbed and weakly chemisorbed N_2O can be easily desorbed even at low temperature (<473 K) with only stronger absorbed species left. At higher temperatures (>573 K), the disappearance of N_2O infrared bands was mainly caused by the decomposition of remaining chemisorbed N_2O species.

According to the in situ N_2O-DRIFTS studies, the first step for the direct decomposition of N_2O on the Fe-beta zeolite was thought to involve a reversible equation:

$$N_2O(g) + \sigma \leftrightarrow \sigma N_2O, \quad (3.1)$$

where σ represented active center of Fe-beta (noted as Fe-Z) after He pretreatment at high temperature. σN_2O delegated the cluster of Fe-beta with adsorbed N_2O (noted as Fe-Z-N_2O).

Fig. 3C shows NO–N_2O-DRIFT spectra for Fe-beta-1% zeolite with an exposure to N_2O (4 vol% in He) for 1 h at 573 K and then switch to NO (3.99 vol% in He) at 573 K. The bands at 2208–2218 and 2235 cm^{-1} belong to the ν(N–N) stretching modes of N_2O according to our above assignment. The big band at 1387 cm^{-1} was associated with the ν_{as}(NO) stretching of *cis*-$N_2O_2^{2-}$ species [47–49]. The minor band at 1757 cm^{-1} was due to Fe^{n+}-$(NO)_2$ [47]. The bands at 1596 and 1630 cm^{-1} were assigned to the stretch of –NO_2 of chelating nitrate and bridging bidentate nitrate, respectively [50,51]. The generation of adsorbed –NO_2 species provides evidence of the existence of so-called α-O generated from the Fe-beta zeolite after N_2O pretreatment at 573 K.

3.3.2. N_2O-TPD, NO_2-TPD and N_2O-TPSR studies

Fig. 4 shows the N_2O-TPD profile for Fe-beta-1% zeolite pretreated by N_2O (4 vol% in He, 20 ml/min) at 573 K. The mass signal of N_2 was 5-fold reduced, whereas the mass trace of NO_2 was 10-fold magnified for a better comparison with those of other gases. The

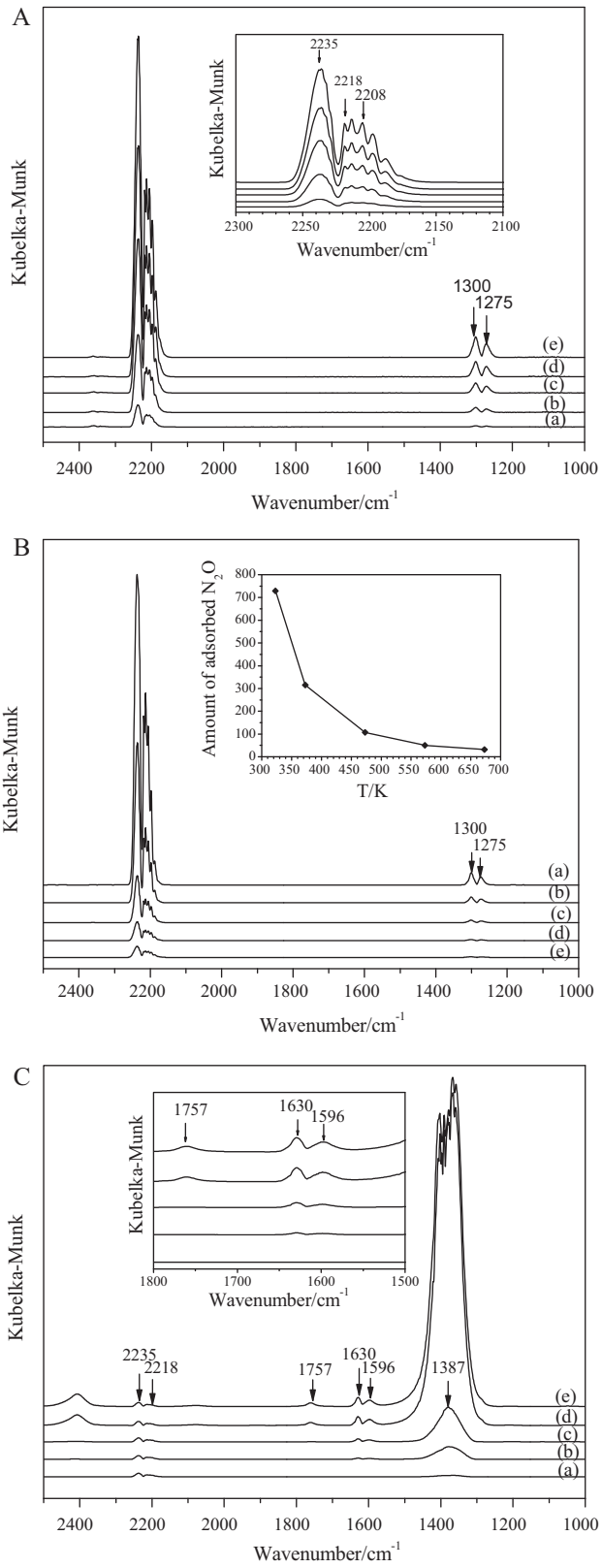

Fig. 3. (A) DRIFTS of Fe-beta-1% zeolite with an exposure to N_2O (4 vol% in He, 20 ml/min) at 573 K for (a) 1 min, (b) 2 min, (c) 3 min, (d) 4 min, (e) 5 min. (B) DRIFTS of Fe-beta-1% zeolite with an exposure to N_2O (4 vol% in He, 20 ml/min) at (a) 323 K, (b) 373 K, (c) 473 K, (d) 573 K, (e) 673 K for 1 h. (C) DRIFTS of Fe-beta-1% zeolite pretreated by 4 vol% N_2O for 1 h at 573 K, with an exposure to NO (3.99% in He, 20 ml/min) at 573 K for (a) 1 min, (b) 2 min, (c) 3 min, (d) 4 min, (e) 5 min.

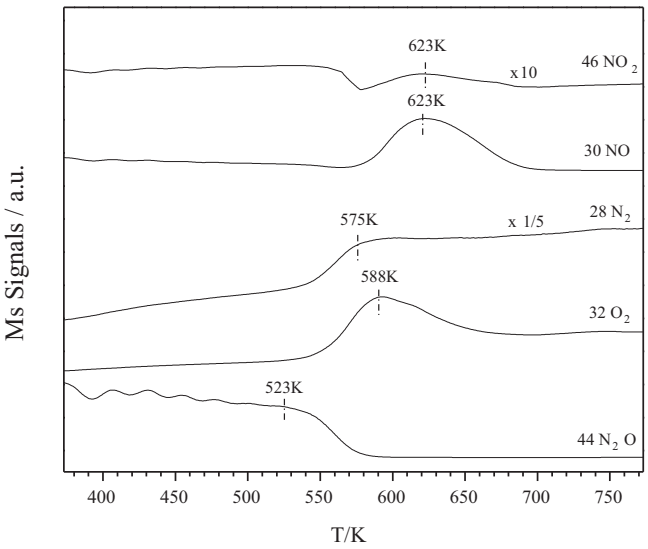

Fig. 4. N_2O-TPD profile for Fe-beta-1% zeolite pretreated by 20 ml/min of 4 vol% N_2O/He at 573 K.

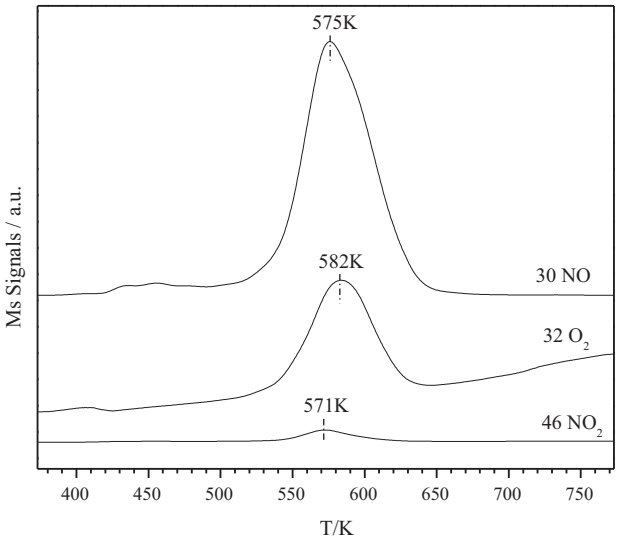

Fig. 5. NO_2-TPD profile for Fe-beta-1% zeolite pretreated by 20 ml/min of 2 vol% NO_2/He at 573 K.

response signal of N_2O dropped rapidly at about 523 K, simultaneously with the appearance of N_2 peak (at 575 K) and O_2 peak (at 588 K). N_2 could be desorbed more easily (exhibiting as a desorption peak at slightly lower temperature) than O_2. The mass signals of both NO and NO_2 were observed with a desorption peak at 623 K, although the uptake of NO_2 was just minor (see Fig. 4).

Based on the DRIFTS and N_2O-TPD results, the generation of N_2 and O_2 was realized via a dissociation of chemisorbed N_2O as formulated by Eqs. (3.2)–(3.4) according to our previous study [52].

$$\sigma N_2O \rightarrow N_2(g) + \sigma O \quad (3.2)$$

$$\sigma O \rightarrow N_2O(g) \rightarrow \sigma O_2 + N_2(g) \quad (3.3)$$

$$\sigma O_2 \rightarrow \sigma + O_2(g) \quad (3.4)$$

Eq. (3.2) formulated the decomposition of the first N_2O over Fe–Z with formation of nitrogen and Fe-O-Z (noted as σO). This oxygen species of Fe-O-Z was the so called α-O. Then, the second N_2O could be decomposed into N_2 and Fe-O_2-Z (noted as σO_2) over Fe-O-Z. It was worth noting that both N_2O participated in above two reactions with O end adsorbing upon the active center Fe of Fe-Z or Fe-O-Z. Finally O_2 was desorbed from Fe-O_2-Z as formulated by Eq. (3.4).

As shown in Fig. 4 the desorption temperature of O_2 (588 K) was higher than that of N_2 (575 K), which revealed that desorption of O_2 would be the rate determining step for N_2O direct decomposition over Fe-beta zeolite.

N_2-TPD was also conducted over Fe-beta-1% zeolite (not shown). It was found that adsorbed nitrogen could be completely removed from the zeolite surface at <373 K, implying that N_2 was mainly physisorbed over the Fe-beta catalyst, resulting in its easy desorption. In addition, this finding is consistent with our assumption that N_2 desorption during N_2O-TPD occurring at around 575 K is caused by N_2O dissociation.

NO and NO_2 appearing in the N_2O-TPD effluent were believed to be generated through the interaction between N_2O and α-O of Fe-O-Z as illustrated by Eqs. (3.5)–(3.7). In Eq. (3.5) N_2O adsorbed upon the α-O with its N end and formed Fe-Z-$(NO)_2$ (noted as σON–NO) which could be dissociated into NO and Fe-Z-NO (noted as σNO) as shown in Eq. (3.6). These reaction pathways were further simulated by our DFT calculations (see Section 3.3.4) and the result was comparable to that reported by Heyden over Fe-ZSM-5 zeolite [35]. Fe-Z-NO seems to be active enough to capture the O from N_2O to yield Fe-Z-NO_2 (noted as σNO_2) through a disproportionation process (Eq. (3.7)).

$$N_2O(g) + \sigma O \rightarrow \sigma ON - NO \quad (3.5)$$

$$\sigma ON - NO \rightarrow \sigma NO + NO(g) \quad (3.6)$$

$$\sigma NO + N_2O(g) \rightarrow \sigma NO_2 + N_2(g) \quad (3.7)$$

Subsequently, the adsorbed NO_2 was able to be desorbed from Fe-Z-NO_2 as shown in Fig. 4 with a small signal of NO_2 and formulated by:

$$\sigma NO_2 \rightarrow NO_2(g) + \sigma \quad (3.8)$$

As further investigation, we also investigated NO_2-TPD with a similar procedure as that for N_2O-TPD except that the pretreating gas was substituted into NO_2 (2 vol% in He) as shown in Fig. 5. It was found that the signals of NO, O_2 and NO_2, were all detectable at almost the same temperature range from 513 to 673 K which suggested that NO_2 could be catalytic decomposed over Fe-beta zeolite undergoing the follow pathways.

$$\sigma NO_2 \rightarrow \sigma O + NO(g) \quad (3.9)$$

$$\sigma O + NO_2 \rightarrow \sigma O_2 + NO(g) \quad (3.10)$$

The detection of a small amount of NO_2 revealed that NO_2 could be desorbed from Fe-beta zeolite as formulated in Eq. (3.8). O_2 uptake was observable as addressed by Eq. (3.4).

Temperature programmed surface reaction (TPSR) of N_2O over Fe-beta-1% was depicted in Fig. 6 representing the mass traces of N_2O, N_2, O_2 and NO. The initial decline in the N_2O signal at low temperature region (373–473 K) was likely due to its chemisorption on the catalyst. As the temperature up to 623 K, a sudden drop in the amount of N_2O was clearly seen simultaneously with the increasing mass signals for N_2 and O_2 finally reaching the saturated level. A small amount of NO (with a maximum concentration of 150 ppm taking place at 623 K during N_2O-TPSR) was observed by both MS and infrared gas analyzer. This again confirmed the generation of a NO intermediate during the N_2O dissociation into N_2 and O_2.

3.3.3. *Mechanism summary*

The mechanism of N_2O direct decomposition over Fe-beta zeolite was studied here through the N_2O-TPD, NO_2-TPD, N_2-TPD, N_2O-TPSR and in situ DRIFTS. The interconversion among N_2O, NO

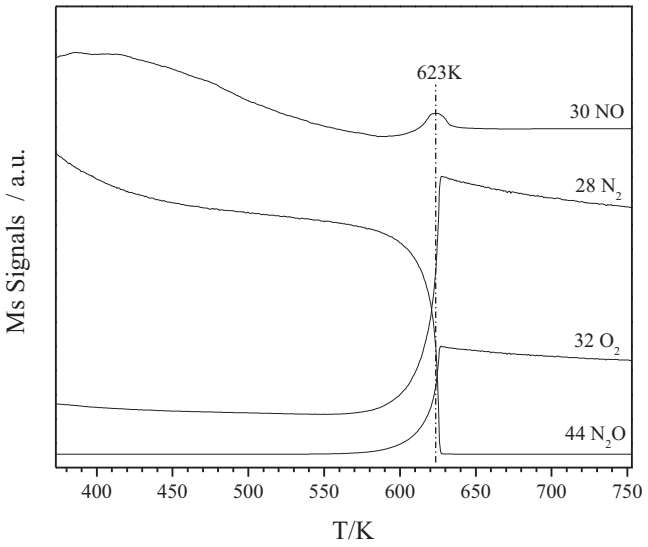

Fig. 6. N_2O-TPSR profile for Fe-beta-1% zeolite, conditions: 35 vol% N_2O/He, GHSV = 4000 h^{-1}, ramp rate = 5 K/min.

and NO_2 as well as the role of NO as an intermediate was thereafter discussed based on the above investigations.

Generally, N_2O direct decomposition over Fe-beta zeolite involves the following steps: N_2O was firstly chemisorbed upon the active site of single ionic Fe^{n+} (σ) ($n < 3$, because of He pretreatment at 773K) on Fe-Z and formed Fe-Z-N_2O (σN_2O). This chemisorbed N_2O was subsequently dissociated into N_2 and Fe-O-Z (σO), accompanying with the rise of temperature. The second N_2O molecule could adsorb on Fe-O-Z in two ways with respective formation of O_2 or NO_x as verified in N_2O-TPD, so that two kinds of reaction mechanisms would be proposed as follows.

For the mechanism with O_2 formation, the second N_2O adsorbed on the Fe active center through its O end with formation of Fe-O-Z-N_2O (noted as Oσ–ON_2) which could be dissociated into N_2 and Fe-O_2-Z (δO_2) as the temperature rose. Then O_2 could be released from Fe-O_2-Z to regenerate Fe-Z (σ) site, which was believe to be the rate limiting step for N_2O decomposition over Fe-beta zeolite [26]. This reaction mechanism was believed to be the dominated mechanism and further studied by means of computational chemistry based on DFT as discussed in the following Section 3.3.4.1.

For the additional mechanism involving NO_x formation, the second N_2O adsorbed on α-O through its N end with the formation of Fe-Z-$(NO)_2$ (σON–NO), which was attributed to the strong activity of α-O. Then, Fe-Z-$(NO)_2$ could be decomposed into Fe-Z-NO (σNO) and nitric oxide (NO). Fe-Z-NO was so active to capture the O from N_2O, yielding the Fe-Z-NO_2 (σNO_2) through a disproportionation process. Thereafter, the following reaction mechanism could be recognized as decomposition of NO_2 over Fe-Z zeolite into Fe-O-Z (σO) and NO. For this mechanism, the formation of NO as formulated in Eqs. (3.5) and (3.6) was successfully simulated by DFT calculations and discussed in detail in Section 3.3.4.2.

These two kinds of reaction mechanisms can be concluded as follows.

The O_2-formation mechanism

$$N_2O(g) + \sigma \leftrightarrow \sigma N_2O$$
$$\sigma N_2O \rightarrow N_2(g) + \sigma O$$
$$\sigma O + N_2O(g) \leftrightarrow O\sigma\text{-}ON_2$$
$$O\sigma\text{-}ON_2 \rightarrow \sigma O_2 + N_2(g)$$
$$\sigma O_2 \rightarrow O_2(g) + \sigma$$
$$N_2O(g) \rightarrow N_2(g) + O_2(g)$$

The NO_x-formation mechanism

$$\sigma O + N_2O(g) \leftrightarrow \sigma ON\text{-}NO$$
$$\sigma ON\text{-}ON \rightarrow \sigma NO + NO(g)$$
$$\sigma NO + N_2O(g) \rightarrow \sigma NO_2 + N_2(g)$$
$$\sigma NO_2 \rightarrow \sigma O + NO(g)$$
$$2N_2O(g) \leftrightarrow 2NO(g) + N_2(g)$$

3.3.4. DFT calculations on N_2O decomposition over 5T-Fe-beta zeolite

3.3.4.1. Mechanism with formation of O_2. The N_2O decomposition mechanism with O_2 formation over Fe-beta zeolite was further studied by employing computational chemistry based on density functional theory (DFT) in this section. This decomposition mechanism simulated over 5T-Fe-beta zeolite model includes three parts and nine reaction steps as listed in Scheme 1. Part A1 formulates a decomposition of the first N_2O molecule over Fe-Z with the formation of N_2 and Fe-O-Z. Part A2 shows the subsequent decomposition of the second N_2O molecule over Fe-O-Z with another N_2 generation and Fe-O_2-Z. Part A3 describes the O_2 desorption from Fe-O_2-Z. The models used in these three parts were illustrated in Fig. 7 with their optimized geometrical parameters being reported in Table 2 of Part A in which the atom numbers were also labeled as shown in Fig. 7. Energy profiles of Part A1 and Part A2 represent in Fig. 8a, while the energy profile of Part A3 was not shown for the sake of brevity. Data of energy barriers and reaction enthalpies of each reaction step were listed in Table 3 of Part A.

For Step A1 with the formation of adsorbed N_2O (Fe-Z-N_2O) on Fe-Z, the adsorption energy was −13.18 kcal/mol and the enthalpy of reaction (ΔH_r) was −12.62 kcal/mol, which revealed that N_2O could easily adsorbed on Fe-Z without energy barrier and with some heat releasing. Because of the low energy barrier the reverse reaction could also occur at the reaction temperature, which agrees well with the result obtained from the in situ N_2O-DRIFTS. Through the frequency calculation over 5T-Fe-Z-N_2O model, two frequencies associated with ν(N–O) and ν(N–N) were found with values of 1280 and 2240 cm^{-1}, respectively, which were in accordance with the former in situ N_2O-DRIFT study (Fig. 3A and B).

Step A2, showing the transform from the adsorbed state (Fe-Z-N_2O) to the transition state (Fe-Z-N_2O-TS), was the main reaction

Part A1	
Fe-Z+N_2O→Fe-Z-N_2O	(1) Step A1
Fe-Z-N_2O→Fe-Z-N_2O-TS	(2) Step A2
Fe-Z-N_2O-TS→Fe-O-Z-N_2	(3) Step A3
Fe-O-Z-N_2→Fe-O-Z+N_2	(4) Step A4
Fe-Z+N_2O→Fe-O-Z+N_2	(5) Whole Reaction of Part A1
Part A2	
Fe-O-Z+N_2O→Fe-O-Z-N_2O	(6) Step A5
Fe-O-Z-N_2O→Fe-O-Z-N_2O-TS	(7) Step A6
Fe-O-Z-N_2O-TS→Fe-O_2-Z-N_2	(8) Step A7
Fe-O_2-Z-N_2→Fe-O_2-Z+N_2	(9) Step A8
Fe-O-Z +N_2O→Fe-O_2-Z+N_2	(10) Whole Reaction of Part A2
Part A3	
Fe-O_2-Z →Fe-Z+O_2	(11) Step A9

Scheme 1. Reaction steps of mechanism with O_2 formation.

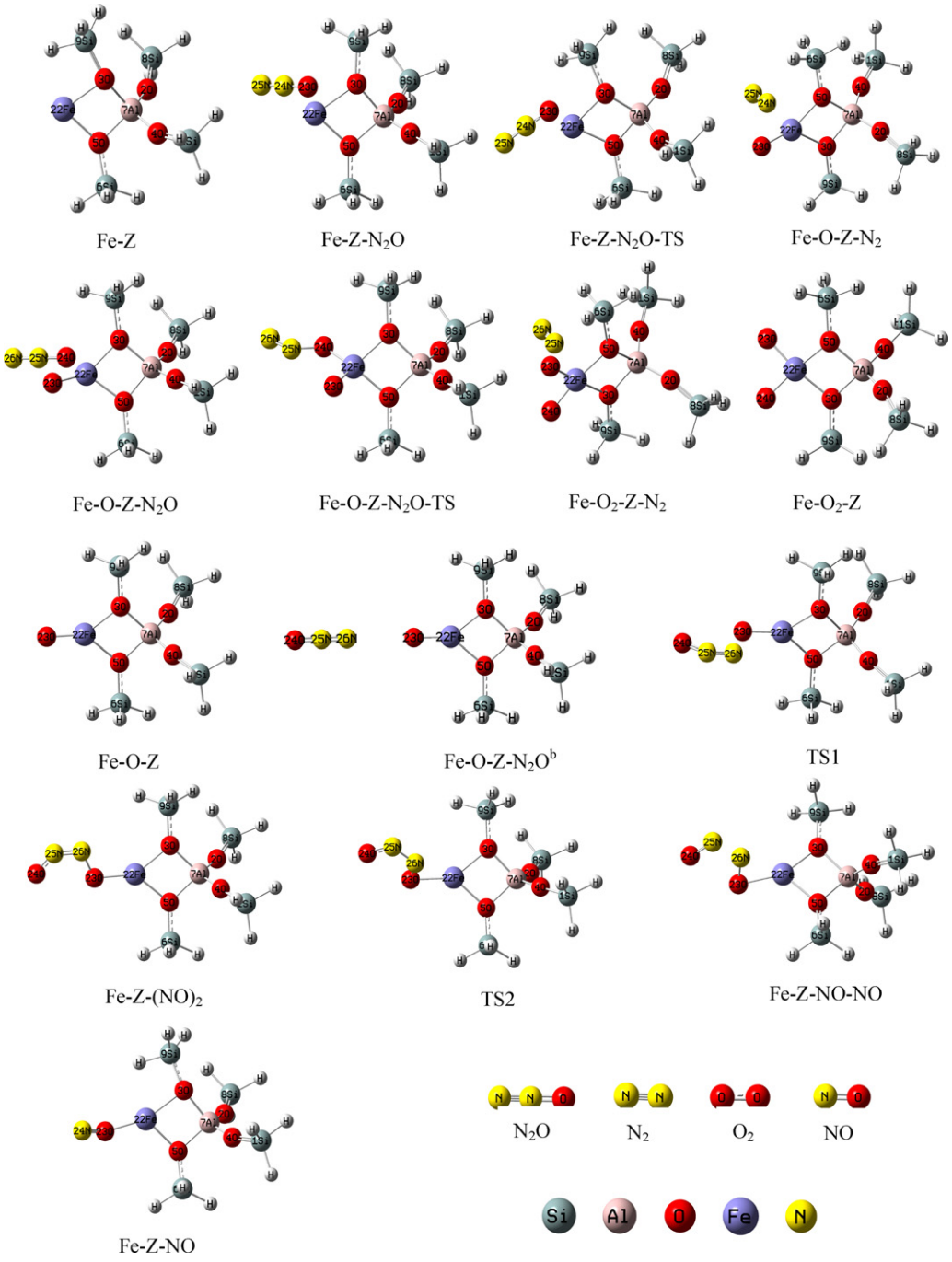

Fig. 7. Optimized models used in DFT calculations.

step which determined the activation barrier of Part A1. The transition state Fe-Z-N_2O-TS is characterized by a Fe–O (atom O of N_2O) bond distance of 2.259 Å, O–N′ (the middle N of N_2O) bond distance of 1.226 Å, N′–N″ bond distance of 1.137 Å and the bending of N_2O molecule from 180° in the adsorbed state to 163.6° in the transition state. The imaginary frequency associated with the transition-state mode is 489i cm^{-1}. This transition state was also testified by IRC calculations. As shown in Table 3 an activation barrier of Step A2 was only 8.94 kcal/mol associated with a ΔH_r of 9.08 kcal/mol, which replied that decomposition of the first N_2O molecule on Fe-Z was endothermic with the easy formation of N_2 and α-O.

Step A3 involves a change from the transition state (Fe-Z-N_2O-TS) to the product state (Fe-O-Z-N_2), with energy barrier of −74.60 kcal/mol and the enthalpy of −73.65 kcal/mol, which revealed that this process released lots of heat with no energy barrier. The desorption of N_2 from Fe-O-Z-N_2 was formulated as Step A4 with a relatively small energy barrier of 1.89 kcal/mol and ΔH_r of 2.81 kcal/mol, suggesting that N_2 could be easily desorbed from Fe-O-Z when a small amount of energy was offered. This is consistent with the observation in N_2-TPD (not shown) that N_2 was able to be desorbed from Fe-beta zeolite at relatively low temperature (<373 K).

Energy calculations for the Overall Reaction of Part A1 were also studied. Due to the existence of a transition state, the general energy barrier of Part A1 reported in Table 3 was not the real energy barrier for the whole reaction; it was calculated to show

Table 2
Optimized geometrical parameters (distances in Å, angles in°) of models used in DFT calculations.

Part A1

Model	Al-O3	Al-O5	Al-O2	Al-O4	Fe-O3	Fe-O5	Fe-O23	O23-N24	N24-N25	–	–	∠O23-N24-N25
Fe-Z	1.828	1.834	1.711	1.707	2.117	2.028	–	–	–	–	–	–
Fe-Z-N_2O	1.808	1.829	1.712	1.709	2.231	2.041	2.757	1.202	1.131	–	–	180.0
Fe-Z-N_2O-TS	1.819	1.839	1.710	1.709	2.140	1.991	2.259	1.226	1.137	–	–	163.6
Fe-O-Z-N_2	1.846	1.845	1.710	1.716	2.020	2.016	1.671	3.143	1.103	–	–	–
Fe-O-Z	1.833	1.844	1.705	1.705	2.082	1.983	1.664	–	–	–	–	–
N_2O	–	–	–	–	–	–	–	1.185	1.125	–	–	180.0
N_2	–	–	–	–	–	–	–	–	1.105	–	–	–

Part A2

Model	Al-O3	Al-O5	Al-O2	Al-O4	Fe-O3	Fe-O5	Fe-O23	Fe-O24	O23-O24	O24-N25	N25-N26	∠O24-N25-N26
Fe-O-Z-N_2O	1.846	1.846	1.713	1.711	2.026	2.013	1.672	2.307	2.978	1.210	1.125	180.0
Fe-O-Z-N_2O-TS	1.847	1.859	1.706	1.706	2.014	1.940	1.624	1.839	2.770	1.405	1.159	129.1
Fe-O_2-Z-N_2	1.842	1.840	1.708	1.713	1.971	1.975	1.675	1.676	2.307	3.137	1.103	–
Fe-O_2-Z	1.849	1.846	1.708	1.708	1.953	1.955	1.673	1.675	2.311	–	–	–
O_2	–	–	–	–	–	–	–	–	1.216	–	–	–

Part B1

Model	Al-O3	Al-O5	Al-O2	Al-O4	Fe-O3	Fe-O5	Fe-O23	O23-N26	N26-N25	N25-O24		∠O24-N25-N26
Fe-O-Z-N_2O[b]	1.851	1.850	1.710	1.712	2.008	2.000	1.660	3.155	1.134	1.194	–	180.0
TS1	1.854	1.847	1.711	1.712	2.004	2.007	1.783	1.678	1.185	1.211	–	149.9
Fe-Z-$(NO)_2$	1.849	1.840	1.711	1.713	2.012	2.025	1.833	1.394	1.241	1.229	–	133.0

Part B2

Model	Al-O3	Al-O5	Al-O2	Al-O4	Fe-O3	Fe-O5	Fe-O23	O23-N26	N26-N25	N25-O24		∠O24-N25-N26
TS2	1.846	1.851	1.710	1.711	2.010	1.991	1.958	1.336	1.328	1.227	–	119.4
Fe-Z-NO-NO	1.843	1.849	1.709	1.709	2.002	1.991	2.019	1.308	1.438	1.206	–	112.9

Part B3

Model	Al-O3	Al-O5	Al-O2	Al-O4	Fe-O3	Fe-O5	Fe-O23	O23-N24	–	–	–	–
Fe-Z-NO	1.835	1.823	1.708	1.707	2.063	2.023	1.889	1.223	–	–	–	–
NO	–	–	–	–	–	–	–	1.159	–	–	–	–

the energy difference between the initial reactants and the final products of Part A1. The total ΔH_r of Part A1 was −74.38 kcal/mol, indicating that the direct decomposition of the first N_2O molecule over Fe-Z was a strongly exothermic process.

Reaction Step A5 described an adsorption of the second N_2O molecule on Fe-O-Z formed in Step A4. The adsorption energy was −5.65 kcal/mol, while the reaction enthalpy ΔH_r was −6.74 kcal/mol. It revealed that no energy barrier existed in this reaction step and N_2O could easily adsorbed on Fe-O-Z with a small amount of heat release. As noted, the reverse reaction could also occur at reaction temperature.

The transformation from the adsorbed state of Fe-O-Z-N_2O to the transition state of Fe-O-Z-N_2O-TS (formulated as Step A6) was regarded as the main reaction step of Part A2, because the general activation barrier of Part A2 was essentially determined by the activation barrier of 35.78 kcal/mol for Step A6, which was com-

Table 3
Energy calculations for each reaction step in DFT calculations.

	Reaction steps	[a] E/kcal mol^{-1}	[b] ΔH_r/kcal mol^{-1}
Mechanism with O_2 formation (Part A)	StepA1	−13.18	−12.62
	Step A2	8.94	9.08
	Step A3	−74.60	−73.65
	Step A4	1.89	2.81
	Overall reaction of Part A1	−76.95	−74.38
	Step A5	−5.65	−6.74
	Step A6	35.78	36.31
	Step A7	−44.61	−44.68
	Step A8	4.62	2.74
	Overall reaction of Part A2	−9.86	−12.36
	Step A9	63.20	64.80
Mechanism with NO formation (Part B)	Step B1	0.39	−0.62
	Step B2	26.92	27.70
	Step B3	−10.83	−10.14
	Step B4	2.54	1.78
	Step B5	−2.26	−0.68
	Step B6	8.45	9.93

[a] Energy barrier calculated as energy relative difference between product and reactant in each reaction step.
[b] Reaction enthalpy.

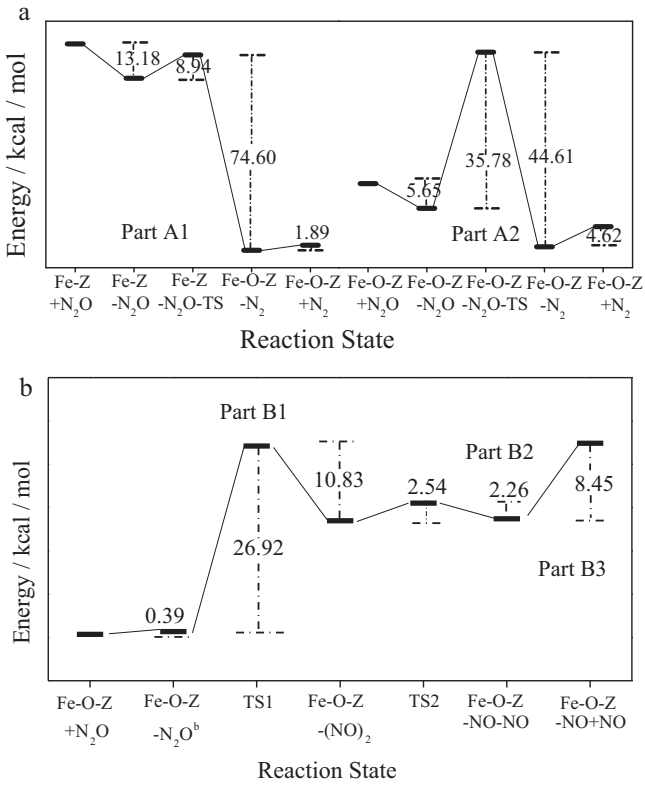

Fig. 8. (a) Energy profile for mechanism with formation of O_2 over 5T-Fe-beta model. (b) Energy profile for mechanism with formation of NO over 5T-Fe-beta model.

parable to the value of 44.2 kcal/mol achieved based on Fe-ZSM-5 zeolite as reported in the literature [53]. The reaction enthalpy (ΔH_r) of Step A6 was calculated to be 36.31 kcal/mol, implying that this step was endothermic. The transition state Fe-O-Z-N_2O-TS was characterized by a Fe-O′ (atom O of the first N_2O) bond distance of 1.624 Å, Fe-O″ (atom O of the second N_2O) bond distance of 1.839 Å, O–N′ (the middle N of N_2O) bond distance of 1.405 Å, N′–N″ bond distance of 1.159 Å and the bending of N_2O molecule from 180° in the adsorbed state to 129.1° in the transition state. The imaginary frequency associated with the transition-state mode is 800i cm^{-1}. This transition state was also testified by IRC calculations.

Step A7 showed the conversion from the transition state of Fe-O-Z-N_2O-TS to the product state of Fe-O_2-Z-N_2 with an energy barrier of −44.61 kcal/mol and a reaction enthalpy of −44.68 kcal/mol. It was similar to Step A3 of Part A1 that the reaction would quickly occur without an energy barrier and release large amount of heat as soon as the energy barrier of the former reaction step was crossed. In Step A8, N_2 was desorbed from Fe-O_2-Z-N_2 showing energy barrier of 4.62 kcal/mol and ΔH_r of 2.74 kcal/mol, suggesting that N_2 could be easily desorbed from Fe-O_2-Z.

For the Overall Reaction of Part A2 it could be found that the energy difference between initial reactants and final products was 9.86 kcal/mol and the general reaction enthalpy was −12.36 kcal/mol, implying that the second N_2O molecule decomposition over Fe-O-Z in Part A2 was exothermic.

Step 9 of Part A3 illustrates the process of O_2 desorption from Fe-O_2-Z. The energy barrier of this reaction step was as much as 63.20 kcal/mol, while the reaction enthalpy (ΔH_r) was 64.80 kcal/mol. The present value of energy barrier of 63.20 kcal/mol was comparable to the reported theoretical values of 67.3 kcal/mol [32], 54.2 kcal/mol [34] and 51.9 kcal/mol [54] over Fe-ZSM-5 zeolites.

Part B1

Fe-O-Z+N_2O(g)→Fe-O-Z-N_2O^b	(1) Step B1
Fe-O-Z-N_2O^b→TS1	(2) Step B2
TS1→Fe-Z-$(NO)_2$	(3) Step B3
Part B2	
Fe-Z-$(NO)_2$→TS2	(4) Step B4
TS2→Fe-Z-NO-NO	(5) Step B5
Part B3	
Fe-Z-NO-NO→Fe-Z-NO+NO(g)	(6) Step B6

Scheme 2. Reaction steps of mechanism with NO formation.

Based on the energy calculations for these nine reaction steps it could be easily found that desorption of O_2 was the rate-limiting step for N_2O decomposition over Fe-beta zeolite, which was in accordance with the present experiment results as mentioned in Section 3.3.3, and with the literature [26]. Reaction enthalpy calculations indicated that Part A1 and Part A2, processes of decomposition of N_2O molecule with O_2 formation, were exothermic processes. Part A3 for the desorption of O_2 was however a strongly endothermic process needing a large amount of energy.

3.3.4.2. Mechanism with formation of NO. In this section the mechanism with NO formation, as formulated in Eqs. (3.5) and (3.6), was successfully simulated by DFT calculations. Moreover, the mechanism with NO formation was summarized as three parts and six reaction steps as listed in Scheme 2. Part B1 depicted the formation of Fe-Z-$(NO)_2$. Part B2 described the transformation from Fe-Z-$(NO)_2$ to the product state of Fe-Z-NO-NO. The desorption of nitric oxide (NO) from Fe-Z-NO-NO was formulated in Part B3. For this section the models with the atom numbers labeled were also shown in Fig. 7 and the optimized geometrical parameters of the models were listed in Table 2 of Part B. The energy profile was depicted in Fig. 8b along with the energy barriers and reaction enthalpies of each reaction step being listed in Table 3 of Part B.

For Part B1, N_2O was firstly adsorbed on α-O of Fe-O-Z through its N end to form Fe-O-Z-N_2O^b with a N-O (α-O) bond length of 3.155 Å and N_2O bond angle of 180°. As shown in Table 3 the energy barrier of this reaction step (Step B1) was only 0.39 kcal/mol, which revealed that this reaction step and its reverse process could occur at the reaction temperature. Then, Fe-O-Z-N_2O^b could be transformed to the first transition state (TS1), as formulated by Step B2, with a reaction energy barrier of 26.92 kcal/mol and a reaction enthalpy of 27.70 kcal/mol, which were close to the values of 28.2 kcal/mol (energy barrier) and 24.4 kcal/mol (ΔH_r) reported by Heyden [35]. The dominant role of Step B2 for Part B1 was believed to be due to its activation barrier. TS1 was characterized by a decrease in bond angle of the N_2O molecule from 180° of adsorbed state to 149.9° of transition state, whereas the N–N′ (N′ was the middle atom N of N_2O) length increased from 1.134 Å to 1.185 Å. The imaginary frequency associated with the transition-state mode is 635.5i cm^{-1}. Step B3 showed the transfer from TS1 to the product state of Fe-Z-$(NO)_2$ with an energy barrier of −10.83 kcal/mol and a reaction enthalpy of −10.14 kcal/mol.

Part B2 represented the transformation of Fe-Z-$(NO)_2$ to Fe-Z-NO-NO through a transition state (TS2). Step B4 of Part B2, from Fe-Z-$(NO)_2$ to the TS2, had an activation barrier of 2.54 kcal/mol and a reaction enthalpy of 1.78 kcal/mol, which revealed that Part B2 could easily occur with the supply of small amount of energy. TS2 was characterized by an increase in the N–N′ bond length from 1.241 Å in Fe-Z-$(NO)_2$ to 1.328 Å in transition state and the bond angle of N_2O decreased from 133.0° to 119.4°. The imaginary fre-

quency associated with the transition-state mode is 507.6i cm^{-1}. Step B5 described the transformation from the state of TS2 to the product state of Fe-Z-NO-NO with energy barriers of −2.26 kcal/mol and −0.68 kcal/mol, respectively.

In Part B3, the desorption of NO from Fe-Z-NO-NO was addressed with the formation of Fe-Z-NO (σNO) and NO associated with the energy barrier of 8.45 kcal/mol and the reaction enthalpy of 9.93 kcal/mol.

Through analysis of the above energy calculations it is clear that Step B2 of Part B1, with the energy barrier of 26.92 kcal/mol, was the main reaction step in mechanism accompanying with NO formation. In other words, the formation of Fe-Z-$(NO)_2$ is the dominant reaction step in this case.

Additionally, it was found that the general energy barriers of NO-formation mechanism with (26.92 kcal/mol) were comparable to that of the O_2-formation mechanism (35.78 kcal/mol), which revealed that N_2O could adsorb upon Fe-O-Z in two ways and both of them could occur under reaction conditions with the respective formation of O_2 or NO.

4. Conclusions

The catalytic activity for N_2O decomposition of bare beta zeolite was obviously enhanced by Fe loading through an ion-exchange process. Nevertheless, no more improvement in *de*N_2O activities was observed along with the loading increase when Fe contents are above 1%. As the ion-exchange content of iron was relatively lower (<1%), the iron mainly existed in ionic Fe^{n+}, which was active for N_2O direct decomposition, on Fe-beta zeolite; while the high Fe loading (>1%) would lead to the aggregation with the formation of FeO_x species, which is less active for N_2O decomposition. The appearance of internal mass transfer control was believed to be another reason for the limited improvement in N_2O conversion upon the further increasing Fe contents.

Two kinds of reaction mechanism with respective formation of O_2 or NO_x intermediate were proposed based on N_2O-TPD, NO_2-TPD, N_2-TPD, N_2O-TPSR, and in situ DRIFTS investigations. Computational chemistry based on density functional theory (DFT) was employed to further study the proposed mechanisms. Energy calculations revealed that O_2 desorption process was the rate determining step in N_2O direct decomposition over Fe-beta zeolite and the energy barriers of 63.2 kcal/mol was comparable to the literature report.

Mechanism with NO formation was also simulated by DFT calculations, and it was found that the formation of Fe-Z-$(NO)_2$ was the main reaction step with the energy barrier of 26.92 kcal/mol. This energy barrier was comparable to that of overall energy barrier of Part A2 in the O_2-formation mechanism (35.78 kcal/mol), which testified that N_2O could adsorb upon Fe-O-Z in two ways and both of them could occur under reaction conditions with respective O_2 or NO formation.

Acknowledgments

The authors thank the National Natural Science Foundation of China under Grant (Nos. 20877007, 20821004, and 20977004), the Research Fund for the Doctoral Program of Higher Education of China (20090010120003), Chinese Universities Scientific Fund (ZZ1003), and the New Century Program for Outstanding Talents in University for the financial support.

References

[1] Inventory of US Green house gases and sinks 1991–1997, EPA, Washington.
[2] J.T. Houghton, IPCC 3rd assessment report. 2001.
[3] M. Galle, D.W. Agar, O. Watzenberger, Chem. Eng. Sci. 56 (2001) 1587.
[4] L. Xue, C.B. Zhang, H. He, Y. Teraoka, Catal. Today 126 (2007) 449.
[5] G.D. Pirngruber, P.K. Roy, R. Prins, J. Catal. 246 (2007) 147.
[6] I. Melián-Cabrera, C. Mentruit, J.A.Z. Pieterse, R.W. van den Brink, et al., Catal. Commun. 6 (2005) 301.
[7] A. Guzmán-Vargas, G. Delahay, B. Coq, Appl. Catal. B 42 (2003) 369.
[8] R.W. van den Brink, S. Booneveld, J.R. Pels, D.F. Bakker, M.J.F.M. Verhaak, Appl. Catal. B 32 (2001) 73.
[9] J.H. Park, J.H. Choung, I.S. Nam, S.W. Ham, Appl. Catal. B 78 (2008) 342.
[10] I. Melián-Cabrera, S. Espinosa, J.C. Groen, B. Linden, F. Kapteijn, J.A. Moulijn, J. Catal. 238 (2006) 250.
[11] J. Pérez-Ramírez, J. Catal. 227 (2004) 512.
[12] J. Pérez-Ramírez, F. Kapteijn, G. Mul, J.A. Moulijn, Appl. Catal. B 35 (2002) 227.
[13] H.A. Xia, K.Q. Sun, Z.M. Liu, Z.C. Feng, P.L. Ying, C. Li, J. Catal. 270 (2010) 103.
[14] G. Delahay, M. Mauvezin, B. Coq, S. Kieger, J. Catal. 202 (2001) 156.
[15] M. Mauvezin, G. Delahay, F. Kisslich, B. Coq, S. Kieger, Catal. Lett. 62 (1999) 41.
[16] S. Kameoka, T. Suzuki, K. Yuzaki, T. Takeda, S. Tanaka, S. Ito, K. Kunimori, S. Miyadera, Chem. Commun. (2000) 745.
[17] Y. Li, J.N. Armor, Appl. Catal. B 1 (1992) L21.
[18] G. Centi, A. Galli, B. Montanari, S. Perathoner, A. Vaccaria, Catal. Today 35 (1997) 113.
[19] G. Centi, S. Perathoner, F. Vazzana, M. Marclla, M. Tomaselli, M. Mantegazza, Adv. Environ. Res. 4 (2000) 325.
[20] L.J. Lobree, I.-C. Wang, J.A. Reimer, A.T. Bell, J. Catal. 186 (1999) 242.
[21] K. Yoshizawa, Y. Shiota, T. Ymura, T. Yamabe, J. Phys. Chem. B 104 (2000) 734.
[22] G.D. Pirngruber, M. Luechinger, P.K. Roy, A. Cecchetto, P. Smirniotis, J. Catal. 224 (2004) 429.
[23] M. Rivallan, G. Ricchiardi, S. Bordiga, A. Zecchina, J. Catal. 264 (2009) 104.
[24] I. Yuranov, D.A. Bulushev, A. Renken, L. Kiwi-Minsker, J. Catal. 227 (2004) 138.
[25] E.V. Kondratenko, J. Pérez-Ramírez, J. Phys. Chem. B 110 (2006) 22586.
[26] K.Q. Sun, H.A. Xia, E. Hensen, R. van Santen, C. Li, J. Catal. 238 (2006) 186.
[27] G.I. Pannov, V.I. Sobolev, A.S. Kharitonov, J. Mol. Catal. 61 (1990) 85.
[28] J. Pérez-Ramírez, F. Kapteijn, G. Mul, J.A. Moulijn, J. Catal. 208 (2002) 211.
[29] A.H. Øygarden, J. Pérez-Ramírez, Appl. Catal. B 65 (2006) 163.
[30] J.A.Z. Pieterse, G.D. Pringruber, J.A. van Bokhoven, S. Booneveld, Appl. Catal. B 71 (2007) 16.
[31] C.R.F. Lund, J. Catal. 243 (2006) 438.
[32] M.F. Fellah, I. Onal, Catal. Today 137 (2008) 410.
[33] A.L. Yakovlev, G.M. Zhidomirov, R.A. van Santen, Catal. Lett. 75 (2001) 45.
[34] A. Heyden, B. Peters, A.T. Bell, F.J. Keil, J. Phys. Chem. B 109 (2005) 1857.
[35] A. Heyden, N. Hansen, A.T. Bell, F.J. Keil, J. Phys. Chem. B 110 (2006) 17096.
[36] R.A. Reimer, C.S. Slaten, M. Seapan, M.W. Lower, P.E. Tomlinson, Environ. Prog. 13 (1994) 134.
[37] W. Kohn, L.J. Sham, Phys. Rev. 140 (1965) A1133.
[38] X.L. Sun, C.P. Huang, B.H. Chen, Acta Phys. -Chim. Sin. 25 (2009) 1136.
[39] M.J. Frisch, G.W. Trucks, H.B. Schlegel, P.M.W. Gill, et al., Gaussian 03, revision B.04, Gaussian, Inc., Pittsburgh, PA, 2003.
[40] W.Y. Lee, R.G. Parr, Phys. Rev. B 37 (1988) 785.
[41] A.D. Becke, Phys. Rev. A 38 (1988) 3098.
[42] G. Munteanu, L. Ilieva, D. Andreeva, Therm. Acta 291 (1997) 171.
[43] G. Berlier, G. Spoto, S. Bordiga, G. Ricchiardi, P. Fisicaro, A. Zecchina, I. Rossetti, E. Selli, L. Forni, E. Giamello, C. Lamberti, J. Catal. 208 (2002) 64.
[44] M.A. Debeila, N.J. Covile, M.S. Surrell, G.R. Hearne, Catal. Today 72 (2002) 79.
[45] B.R. Wood, J.A. Reimer, A.T. Bell, J. Catal. 209 (2002) 151.
[46] G.D. Pirngruber, J.A.Z. Pieterse, J. Catal. 237 (2006) 237.
[47] G.S. Qi, R.T. Yang, Appl. Catal. B 51 (2004) 93.
[48] L. Liu, Y. Chen, L. Dong, J. Zhu, H. Wan, B. Liu, B. Zhao, H. Zhu, K. Sun, L. Dong, Y. Chen, Appl. Catal. B 90 (2009) 105.
[49] B. Azambre, L. Zenboury, F. Delacroix, J.V. Weber, Catal. Today 137 (2008) 278.
[50] Y.W. Chi, S.S.C. Chuang, J. Catal. 190 (2000) 75.
[51] B. Wichterlová, Z. Sobalik, A. Vondrová, Catal. Today 29 (1996) 149.
[52] R. Zhang, H. Alamdari, S. Kaliaguine, J. Catal. 242 (2006) 241.
[53] B.R. Wood, J.A. Reimer, A.T. Bell, M.T. Janicke, K.C. Ott, J. Catal. 224 (2004) 148.
[54] J.A. Ryder, A.K. Chakraborty, A.T. Bell, J. Phys. Chem. B 106 (2002) 7059.